TITLE:

Estimation of Autocorrelation Function and Spectrum Density of Wave-induced Responses Using Prolate Spheroidal Wave Functions

AUTHOR(s):

Tomoki Takami[*1], Ulrik Dam Nielsen[*2,3], and Jørgen Juncher Jensen[*2]

*1 National Maritime Research Institute, Japan

*2 Technical University of Denmark, Denmark

*3 Centre of Autonomous Marine Operations and Systems, NTNU AMOS, Norway

E-mail: takami-t@m.mpat.go.jp

KEYWORDS:

Autocorrelation, Wave-induced Response, Ship Motion, Prolate Spheroidal Wave Functions

ABSTRACT:

Predicting the wave-induced response in the near-future is of importance to ensure safety of ships. To achieve this target, a possible method for deterministic and conditional prediction of future responses utilizing measured data from the most recent past has been developed. Herein, accurate derivation of the autocorrelation function (ACF) is required. In this study, a new approach for deriving ACFs from measurements is proposed by introducing the Prolate Spheroidal Wave Functions (PSWF). PSWF can be used in two ways: fitting the measured response itself or fitting the sample ACF from the measurements. The paper contains various numerical demonstrations, using a stationary heave motion time series of a containership, and the effectiveness of the present approach is demonstrated by comparing with both a non-parametric and a parametric spectrum estimation method; in this case, Fast Fourier Transformation (FFT) and an Auto-Regressive (AR) model, respectively. The present PSWF-based approach leads to two important properties: (1) a smoothed ACF from the measurements, including an expression of the memory time, (2) a high frequency resolution in power spectrum densities (PSDs). Finally, the paper demonstrates that a fitting of the ACF using PSWF can be applied for deterministic motion predictions ahead of current time.

1. INTRODUCTION

Predicting the wave-induced responses that a ship will encounter in the near-future is important to support ship operation. For instance, various marine operations, such as a helicopter landing on the deck of a ship, and crane and maintenance operations (on deep water) of offshore installations, would benefit highly by a deterministic prediction of the future vessel responses expected a short period (less than a minute) ahead of time. The prediction methods developed in past studies are roughly classified in two categories; (a) those

using the wave-excitation input and a hydrodynamic model, e.g. [1], or (b) methods using the correlation structure in the response itself (e.g. AR models), *without* the need of wave input. As regards (a), although time-domain numerical methods for computing wave-induced responses have matured, it is still hard to evaluate the response efficiently on board, as the input of the wave elevation sequence, together with design information of the ship, will be required. Thus, utilizing *just* the on-board measurements are ideal in order to achieve real-time prediction.

As pointed out, AR models, e.g. [2], are useful methods because they do not require input about the waves. Recent researches have shown that the AR models are capable of predicting non-stationary wave-induced responses [3,4]. However, it is critical that the model parameters need to be updated every time the predictions are initiated, and another drawback relates to the amount of training data, which prohibits real-time prediction because of too low computational efficiency [5]. Due to the remarkable advances of recent artificial intelligence technology, machine learning techniques have been developed and applied for achieving real-time prediction of waves and wave-induced responses. Sclavounos and Ma [6] and Ma et al. [7] applied the Support Vector Machine (SVM) regression algorithm for wave elevation forecast. The studies introduced the Gaussian kernel in SVM algorithm to provide robust and analytical solutions in solving inversion of large matrices for training the SVM algorithm. Most recently, Duan et al. [8] addressed the deterministic prediction of nonlinear ship motion by using a Long-Short-Term-Memory (LSTM) deep learning model. The nonlinear effect in the LSTM application was demonstrated. Notwithstanding the effectiveness and impressive performance of the machine learning techniques, some sort of offline training processes are vital to get a reliable prediction model, and there is no consistent way to decide the time length required for training.

Andersen et al. [9] and Nielsen et al. [10,11] investigated and demonstrated a different approach for deterministic response prediction, using the measured autocorrelation function (ACF). This method is based on an assumption that the response ahead of time follows the expected mean variation of the conditional process, considering its prior values. Consequently, stationary processes are assumed. In Ref. [10], the prediction accuracy of ship motion under stationary sea states is demonstrated using the ACF from inverse Fourier transform of the power spectrum density (PSD) from measured ship motion. This ACF-based prediction method neither requires input of the wave/sea conditions, nor does it require offline training, and it has been proved to provide fast and, in many cases, fairly accurate prediction 2-4 wave periods ahead. On the full scale side, a prediction horizon of 2-4 wave periods corresponds to 15-60 [s]. The ACF-based method is able to make predictions in real time, thus it allows the operator for instantaneous update of the prediction results. Besides, the method has the element of hydrodynamic memory time inherently built-in, as the ACF directly expresses the underlying memory time in the response. The main concern of this method is that, in principle, it is not useful for non-stationary responses. As the real sea state, even on relatively short time scales [12], is non-stationary, it is ideal to obtain ACF and PSD from the shortest possible measurement period. In addition, maneuvering effect, i.e. changes in ship speed and heading relative to the

waves, will also introduce a kind of non-stationary behaviour in the wave-induced responses.

The typical ACF of waves or wave-induced responses indicates a curve with a decaying envelope, i.e. it converges to zero up to the memory time. Thus, to achieve reliable prediction based on the ACF-based approach, an estimate of the memory time is necessary; otherwise the prediction accuracy will be deteriorated [10]. However, direct use of sample ACF is not reliable, since the practical measured signal is discretized and the measurement time window is limited, see Box et al. [13]. Therefore, a smoothing process is necessary by using the PSD estimation method such as Fast Fourier Transform (FFT). But, there is no consistent way to choose the smoothing parameters in FFT, e.g. window function or overlap period, to derive the proper ACF from measurements. Moreover, the FFT requires sufficiently long-time measurements to keep the frequency resolution in PSD high.

Recently, Prolate Spheroidal Wave Functions (PSWF) [14] have been utilized for stochastic ocean wave representation [15,16]. Behind this research trend is the presence of several useful approximate algorithms for numerical derivation of PSWF, presented by e.g. Refs. [17–21]. There are two interesting features of PSWF; PSWF are invariant to a finite and infinite Fourier transform [21], and every bandlimited functions can be represented by a linear superposition of PSWF [20–22]. Thus, it is expected that the measured wave-induced response, ACF, and PSD can be explicitly and accurately represented by PSWF. Moreover, the PSWF are capable of achieving a high frequency resolution in PSD as indicated in Refs. [22,23]. Hence, it is also expected to estimate more reliable PSD from short time sequences, allowing estimation during non-stationary periods. Here, it is noteworthy that loads and responses induced in seaways may exhibit considerable ‘non-stationary behaviour’ in the sense that shorter sequences (2-5 minutes) of, say, a 30 minutes time window may show quite varying short-term statistics focused on, for instance, mean, variance, and maximum/minimum values [12]. This so-called short-term variability, as discussed later in the numerical results, is a main argument to study alternative methods for estimation of ACF and PSD.

This paper presents the first step towards achieving a consistent prediction of wave-induced responses based on short-term measurements. A new method for evaluating ACF and PSD of wave-induced responses is presented. The PSWF are introduced to evaluate them in two ways: fitting the time series measurements themselves or fitting the sample ACF from the measurements. Various numerical demonstrations are made by using a simulated heave motion time series of a containership. The effectiveness of the PSWF-based approach is demonstrated by comparing with other spectrum estimation methods. Then, the present PSWF-based approach is applied to the ACF-based deterministic motion prediction [10] of heave motion. Finally, conclusions are stated and possible further applications of the PSWF-based approach are presented.

2. PSWF-BASED EXPRESSION OF ACF AND PSD

2.1. Fitting of Time Series Measurements by PSWF (Method 1)

As the wave-induced response of a ship will be regarded as a band-limited signal, the time series measurements $x(t)$ within the time range of $-T \le t \le T$ can be represented by a linear superposition of

PSWF [15],

$$x(t) \cong x_{PSWF}(t) = \sum_{j=0}^{N_e} a_j \psi_j\left(\frac{t}{T}, c\right), \qquad -T \le t \le T \tag{1}$$

Here ψ_j denote the PSWF, c the Slepian frequency [14], and N_e the number of PSWF to be considered. The numerical derivation of PSWF is described in Appendix A. The coefficients a_j can be estimated by least-squares approach, minimizing

$$F \equiv \int_{-T}^{T} (x(t) - x_{PSWF}(t))^2 dt \tag{2}$$

As

$$\int_{-T}^{T} \left(x_{PSWF}(t)\right)^2 dt = T \sum_{i=0}^{N_e} \sum_{j=0}^{N_e} a_i a_j \int_{-1}^{1} \psi_i(\frac{t}{T}) \psi_j(\frac{t}{T}) d\frac{t}{T} = T \sum_{j=0}^{N_e} a_j^2 \tag{3}$$

due to the orthogonality of the PSWF [21], then

$$\begin{aligned} &\frac{\partial F}{\partial a_j} = 0 \\ &\rightarrow a_j = \int_{-1}^{1} \psi_j\left(\frac{t}{T}, c\right) x\left(\frac{t}{T}\right) d\frac{t}{T} \end{aligned} \tag{4}$$

The discretized values of PSWF are derived with equidistant values of dt/T=0.001 as per the procedure described in Appendix A. The Fourier invariance of PSWF [21] indicates the following relationships,

$$\begin{aligned} &\sum_{\substack{j=0 \\ j\ even}}^{N_e} \psi_j(\frac{t}{T}, c) = \sum_{\substack{j=0 \\ j\ even}}^{N_e} \frac{1}{\lambda_j} \int_{-1}^{1} \psi_j(\frac{\omega}{\Omega}, c) \cos\left(c \frac{t}{T} \frac{\omega}{\Omega}\right) d\frac{\omega}{\Omega} \\ &\sum_{\substack{j=0 \\ j\ odd}}^{N_e} \psi_j(\frac{t}{T}, c) = \sum_{\substack{j=0 \\ j\ odd}}^{N_e} \frac{1}{\lambda_j} \int_{-1}^{1} \psi_j(\frac{\omega}{\Omega}, c) \sin\left(c \frac{t}{T} \frac{\omega}{\Omega}\right) d\frac{\omega}{\Omega} \end{aligned} \tag{5}$$

where λ_j denote the scaled eigenvalues of PSWF, see Appendix A. Ω denotes the upper limit of angular frequency which satisfies the following relationship [14]

$$c = T\Omega \tag{6}$$

Then, the Fourier transform of x_{PSWF} can be given as:

$$\begin{aligned} x_{PSWF}(t) &= \sum_{\substack{j=0 \\ even}}^{N_e} \frac{a_j}{\lambda_j} \int_{-1}^{1} \psi_j\left(\frac{\omega}{\Omega}, c\right) \cos\left(c\frac{t}{T}\frac{\omega}{\Omega}\right) d\frac{\omega}{\Omega} + \sum_{\substack{j=0 \\ odd}}^{N_e} \frac{a_j}{\lambda_j} \int_{-1}^{1} \psi_j\left(\frac{\omega}{\Omega}, c\right) \sin\left(c\frac{t}{T}\frac{\omega}{\Omega}\right) d\frac{\omega}{\Omega} \\ &= \int_{-\Omega}^{\Omega} \left[\sum_{\substack{j=0 \\ even}}^{N_e} \frac{a_j}{\Omega\lambda_j} \psi_j\left(\frac{t}{T}, c\right) \cos(\omega t) + \sum_{\substack{j=0 \\ odd}}^{N_e} \frac{a_j}{\Omega\lambda_j} \psi_j\left(\frac{t}{T}, c\right) \sin(\omega t) \right] d\omega \equiv \int_{-\Omega}^{\Omega} X_{PSWF}(\omega) \{\cos(\omega t) + i\sin(\omega t)\} d\omega \\ &\rightarrow X_{PSWF}(\omega) = \sum_{\substack{j=0 \\ even}}^{N_e} \frac{a_j}{\Omega\lambda_j} \psi_j\left(\frac{t}{T}, c\right) - i \sum_{\substack{j=0 \\ odd}}^{N_e} \frac{a_j}{\Omega\lambda_j} \psi_j\left(\frac{t}{T}, c\right) \end{aligned} \tag{7}$$

The double sided power spectrum density, $S^d_{xx,PSWF}(\omega); -\Omega \le \omega \le \Omega$, is then given explicitly by:

$$\begin{aligned} S^d_{xx,PSWF}(\omega) &= \frac{2\pi}{2T} X_{PSWF}{}^*(\omega) X_{PSWF}(\omega) \\ &= \frac{\pi}{T} \left[\left\{ \sum_{\substack{j=0 \\ even\ j}}^{N_e} \bar{a}_j \psi_j\left(\frac{\omega}{\Omega}, c\right) \right\}^2 + \left\{ \sum_{\substack{j=0 \\ odd\ j}}^{N_e} \bar{a}_j \psi_j\left(\frac{\omega}{\Omega}, c\right) \right\}^2 \right] \end{aligned} \tag{8}$$

where $\bar{a}_j = a_j / \Omega\lambda_j$ and the asterisk denotes the complex conjugate. The one sided PSD, $S_{xx,PSWF}; 0 \le \omega \le \Omega,$ is then

$$S_{xx,PSWF}(\omega) = 2S^d_{xx,PSWF}(\omega) \tag{9}$$

It is well-known that the number of significant PSWF becomes $2c/\pi$, cf. [21] for instance, therefore

$$N_e \le 2c/\pi - 1 \tag{10}$$

is sufficient, otherwise the scaled eigenvalues λ_j become close to zero. Due to the Fourier invariance of PSWF, Eq. (5), a_j will always be proportional to λ_j, and $\bar{a}_j$ will be finite, irrespectively how small all λ_j are. Having said that, however, use of too large N_e value might imply numerical instability in calculating PSD by Eq. (9). Specifically, as a result of the Legendre polynomials-based approach used in this paper, see Appendix A, λ_{64}=0.1276 for c=100 and λ_{128}=0.0801 for c=200 can be derived, and no numerical instabilities are observed. Therefore, $N_e \le 64$ for c=100 and $N_e \le 128$ for c=200 are used in the

numerical demonstrations considered later.

According to the Wiener–Khinchin theorem, the ACF from the PSWF-based PSD, $S_{xx,PSWF}$, is calculated by making use of $S_{xx,PSWF}; 0 \le \omega \le \Omega$,

$$R_{xx,PSWF}(t) \cong \int_0^{\Omega} S_{xx,PSWF}(\omega)\cos(\omega t)\,d\omega \tag{11}$$

2.2. Fitting of Sample ACF by PSWF (Method 2)

The sample ACF from time series measurements $x(t)$ is defined by

$$R_{xx}(t) = E\left[x(0)x(t)\right] \tag{12}$$

As the ACF is the even function, only the even functions of PSWF are needed for expressing the sample ACF R_{xx} within $0 \le t \le T$, i.e.

$$R_{xx}(t) \cong R_{xx,PSWF}(t) = \sum_{\substack{j=0 \\ j\ even}}^{N_e} b_j \psi_j(\frac{t}{T}, c), \quad 0 \le t \le T \tag{13}$$

The coefficients b_j can be calculated by least-squares approach as is the case in Method 1,

$$b_j = 2\int_0^1 \psi_j\left(\frac{t}{T}, c\right) R_{xx}\left(\frac{t}{T}\right) d\frac{t}{T} \tag{14}$$

Using the PSWF-based ACF $R_{xx,PSWF}$, Eq. (13), the PSD is also explicitly expressed by PSWF, as

$$\begin{aligned} R_{xx,PSWF}(t) &= \sum_{\substack{j=0 \\ j\ even}}^{N_e} b_j \frac{2}{\lambda_j}\int_0^1 \psi_j(\frac{\omega}{\Omega}, c)\cos\left(c\frac{t}{T}\frac{\omega}{\Omega}\right) d\frac{\omega}{\Omega} \\ &= \int_0^{\Omega}\left\{\sum_{\substack{j=0 \\ j\ even}}^{N_e} b_j \frac{2}{\Omega\lambda_j}\psi_j(\frac{\omega}{\Omega}, c)\right\}\cos(\omega t)\,d\omega \cong \int_0^{\Omega} S_{xx,PSWF}(\omega)\cos(\omega t)\,d\omega \\ &\rightarrow S_{xx,PSWF}(\omega) \cong \sum_{\substack{j=0 \\ j\ even}}^{N_e} b_j \frac{2}{\Omega\lambda_j}\psi_j(\frac{\omega}{\Omega}, c) \end{aligned} \tag{15}$$

due to the Fourier invariance of PSWF, Eq. (5), and the Wiener–Khinchin theorem.

3. NUMERICAL DEMONSTRATIONS

3.1. Heave Motion of a Ship

Time series of heave motion under irregular waves are simulated through the combined action of a wave spectrum and the heave transfer function using standard spectral calculations. For practical convenience, the transfer functions are computed by closed form expressions [24,25]. A sample container ship of which principal particulars are given in Table 1 is used. Head sea condition is assumed. The transfer function of heave motion is shown in Fig. 1, and a Pierson-Moskowitz wave spectrum with significant wave height H_s = 3.5 [m] and zero-crossing period T_z = 8.5 [s] is assumed, see Fig. 1. The PSD of the heave motion, later named 'the input PSD', is shown in Fig. 2.

The inverse Fourier transform of the input PSD, hereafter referred to as 'the input ACF', is shown in Fig. 3. In general, the memory time in ACF is defined as; "Lag beyond which the ACF drops to an insignificant value", e.g. referring to Van der Schaar and Chou [26]. In the present study, the memory time of a response is defined as a time length of input ACF enough to represent the input PSD. The PSDs given by different time length of the input ACF are shown by colored lines in Fig. 2. It can be observed that input ACF up to 80 [s] is enough to represent input PSD, which then can be regarded as the memory time of heave motion in this case. In the case of real phenomena, i.e., the PSD is unknown and only a time series is given, there is a possible way to determine the memory time by referring to the 95% confidence interval or so-called 'large-lag standard error' [13] of the sample ACF. This point will be investigated as part of future works.

Using the PSDs in Fig. 2, a time series of heave motion, $x(t)$, can be generated as

$$x(t) = \sum_{i=1}^{M_w} \sqrt{H(\omega_i)\Delta\omega_i}\left(u_i \cos\omega_i t + \overline{u}_i \sin\omega_i t\right) \tag{16}$$

where u_i and $\overline{u}_i$ denote independent standard normal distributed stochastic variables, ω_i are discrete frequencies, $\Delta\omega_i$ is the non-equidistant increment between discrete frequencies, and $H(\omega_i)$ the input PSD. The frequency discretization is made within frequency interval of $0 < \omega_i \le 3[rad/\mathrm{s}]$ discretized into M_w=800 components.

Wave-induced responses typically will show energy density in a range from 0.05 Hz to about 1 Hz; equivalent to where the wave energy density itself is distributed. However, some responses, such as structural (hull girder) vibrations, manifest themselves at the eigen frequencies of the vibrational modes of the hull girder. In principle, this extends the interesting frequency range, and hence the sampling frequency, until infinity. On the other hand, due to aliasing it is customary to sample at a much higher frequency; this is the standard approach to avoid aliasing (e.g., see Bendat and Piersol [27]). Specifically, for ships, it is normal practice to use a sampling frequency of 20-100 Hz, as also used for the sensor installations on the ships studied by Andersen et al. [9] and Nielsen et al. [28]. For these reasons, a time series of 4000 [s] in total is generated at a sampling frequency of 100Hz. The generated heave motion time series is shown in

Fig. 4.

Table 1 Principal particulars of container ship

Ship length	283.8 m
Breadth	42.0 m
Draught	14.0 m
Block coefficient	0.67

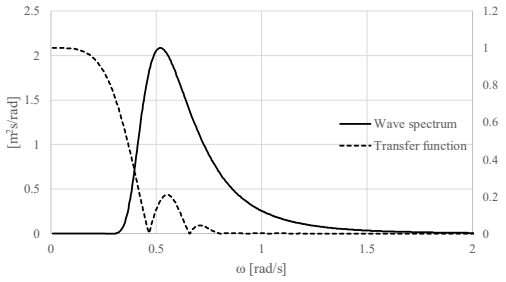

Fig. 1 Transfer function of heave motion and wave spectrum

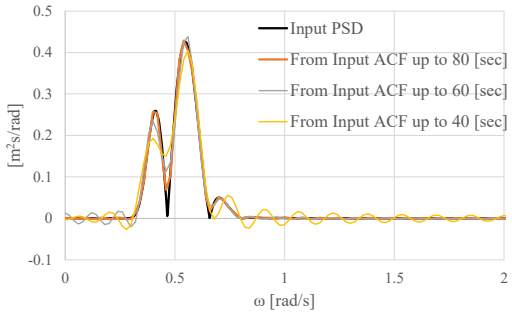

Fig. 2 Power spectral density of heave motion based on transfer function and wave spectrum

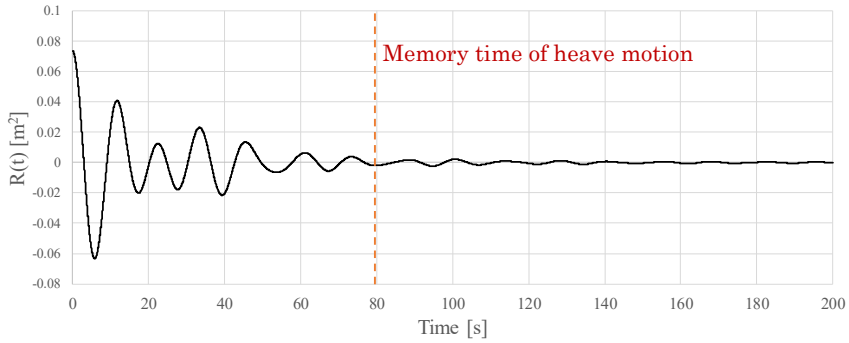

Fig. 3 Inverse Fourier transform of input PSD of heave motion

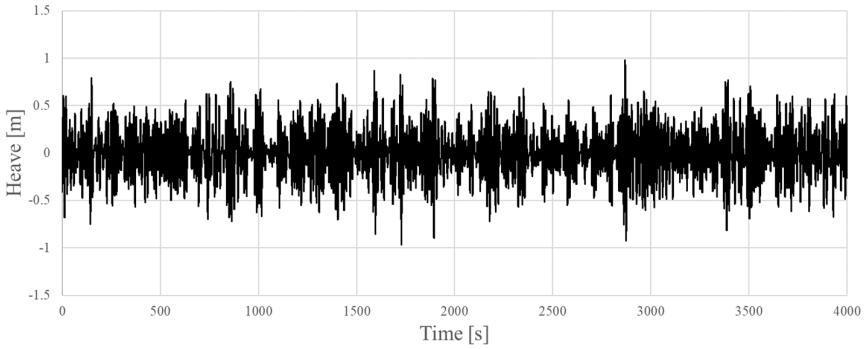

Fig. 4 Heave motion time series

3.2. Estimations of ACF and PSD

3.2.1 Method 1 vs. Method 2

Using an arbitrarily chosen heave motion time series, within $0 \le t \le 100[\mathrm{s}]$, the ACFs and PSDs by Method 1, see Eq. (11) and Eq. (9), respectively, and by Method 2, see Eq. (13) and Eq. (15), respectively, are calculated and compared. The sample ACF of heave motion is calculated according to the following discretized form [29],

$$R_{xx,k} = \frac{1}{M_s} \sum_{m=k+1}^{M_s} (x_m - \mu_x)(x_{m-k} - \mu_x) \tag{17}$$

where μ_x denotes the mean value of discretized heave motion x_m within $0 \le t \le 100[\mathrm{s}]$, M_s the number of sampling. As the sampled frequency is 100Hz, M_s=10001. To obtain the ACF and PSD within 100 sec, c=100, T=50 [s], Ω=2.0 [rad/s] are used for Method 1, while c=100, T=100 [s], Ω=1.0 [rad/s] are used for Method 2. The upper frequency limit Ω=1.0 [rad/s] will be enough to capture the time series and ACF, as the input PSD is band-limited within $0 \le \omega \le 1.0[rad/s]$, see Fig. 2. To fit the time series by discretized PSWF with dt/T=0.001, the heave motion time series is resampled to 20Hz for Method 1, while sample

ACF is resampled to 10Hz.

The ACFs based on Method 1 and Method 2 are shown in Fig. 5. Besides, Fig. 6 provides the PSDs from the two methods. The input PSD, shown as Fig. 2, is included in the plots by gray solid lines. It is clearly seen that the PSD for the 100 [s] segment is much different from the input PSD indicating significant local non-stationary effects. The PSD from the sample ACF is also calculated and plotted in Fig. 6 with dotted lines, by using the following relationship according to the Wiener–Khinchin theorem

$$S_{xx}(\omega) = \frac{2}{\pi}\int_0^T R_{xx}(t)\cos(\omega t)dt \tag{18}$$

As mentioned earlier, N_e=64 is sufficient for c=100. From Fig. 5, when N_e=64 is used, the ACFs from two methods are close to the sample ACF. The difference between Method 1 and Method 2 appears when N_e value is decreased. In the case of Method 1, it can be seen that the ACFs drastically change as N_e decreases. It should be noted that since the ACF value at t=0 [s], i.e. $R_{xx}(0)$, is equal to the variance of signal, mismatch of $R_{xx}(0)$ may lead to the unphysical expression of PSD. In fact, the PSD from Method 1 with N_e=30 indicates unreliable high frequency components, see Fig. 6 a).

When Method 2 is applied, on the other hand, PSWF can express the sample ACF up to a certain time, keeping an accurate $R_{xx}(0)$ expression even if N_e decreases. In other words, by changing N_e values, the ACF are modified so that it converges to zero at an arbitrary time. This is attributed to a fact that only the high-order PSWF are significant to express the ACF where t/T is large. Further, it can be deduced that Method 2 enables to smoothen the PSD by decreasing N_e values, see also Fig. 6 b). It is noted that negative values appear in the estimated PSD when N_e=30 is applied. This is a result from the smoothing of ACF by PSWF. However, the magnitude of the negative values themselves is small, e.g. the area of negative PSD is only about 1% of the total area in the case of N_e=30, and it has been confirmed that the shape of ACF will not change much if the negative components are removed. One may find a mismatch against the input PSD, but such mismatch is unavoidable due to the presence of short-term variability inside the time series. This point will be discussed in Section 3.3. The performance of this kind of smoothing effect by Method 2 is further investigated in the following subsection. From here onward, Method 2 is adopted as the PSWF-based expression of ACF and PSD.

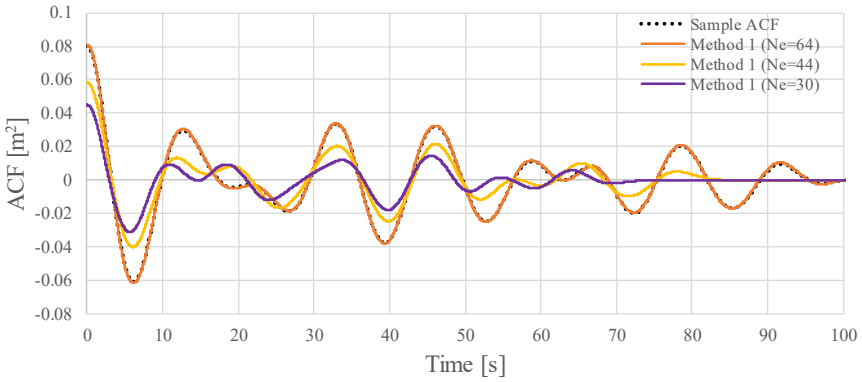

a) Method 1

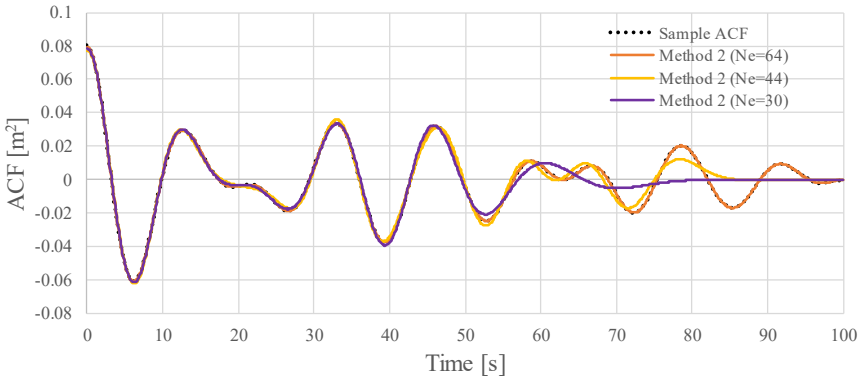

b) Method 2

Fig. 5 ACFs estimated from PSWF-based methods

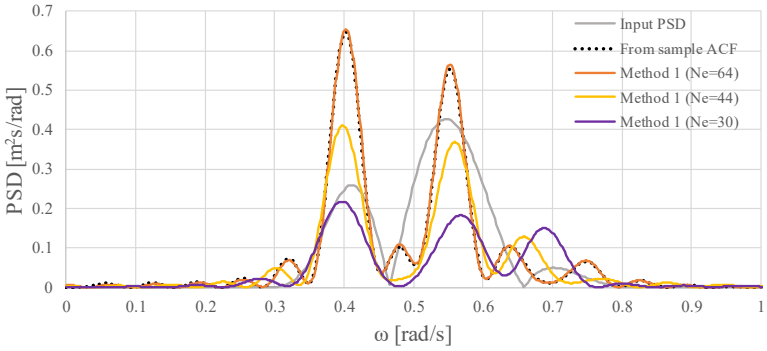

a) Method 1

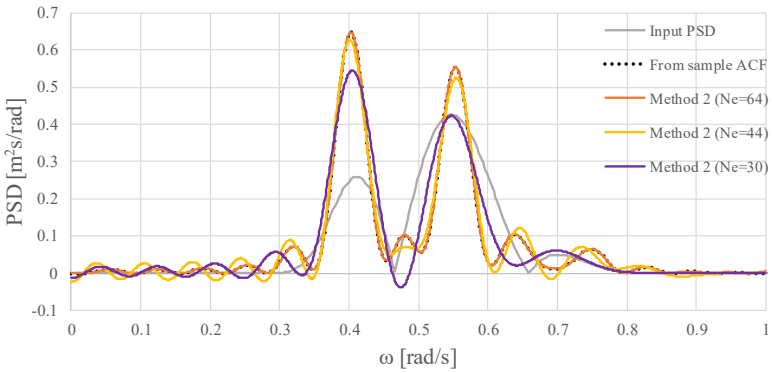

b) Method 2

Fig. 6 PSDs estimated from PSWF-based methods

3.2.2 Smoothing of ACF by Method 2

The convergence time of ACF by Method 2 with different N_e values will now be investigated. Three different cases with different combinations of c, T, and Ω listed in Table 2 are used for a series of examinations. The sample ACFs from $0 \le t \le T$[s] measurements are fitted by Method 2. The ACFs smoothed by Method 2 do not strictly converge to zero and have values at very small digits. In order to investigate the convergence time of ACF by Method 2 consistently, the convergence time *t_conv* is defined as the time over which the ACF converged to 5.0E-7 [m^2] or less, and then the relationships between N_e and *t_conv/T* are plotted in Fig. 7. Results on c=100 (*Case A1*) and c=200 (*Case A2* and *Case A3*) are plotted. *t_conv/T* can be adjusted from 0.4 to 1.0 in *Case A1* and 0.3 to 1.0 in *Case A2* and *Case A3* by changing N_e values. Note that if the same c value is used, *t_conv* represents the similar tendencies, see Fig. 7 b). On the other hand, one should keep in mind that correct representation of $R_{xx}(0)$ by Method 2 is vital, in order for the variance value of the response to be maintained. Fig. 8 shows the relationships between $R_{xx}(0)$ values by Eq. (13) and N_e values for each case. The dotted lines indicate the variance value of the heave response within $0 \le t \le T$[sec]. From the figures, the accuracy of $R_{xx}(0)$ representation is kept for N_e>26 in *Case A1*, N_e>40 in *Case A2*, and N_e>70 in *Case A3*, otherwise the accuracy is deteriorated. By comparing *Case A2* and *Case A3*, smaller N_e can be used for *Case A2* to maintain $R_{xx}(0)$ value with the same value of c. From this result, larger Ω value is ideal to ensure the accuracy for small N_e values.

Table 2 Combination of c, T, and Ω for each case on Method 2

	c (Method 2)	T [s]	Ω [rad/s]
Case A1	100	100	1.0
Case A2	200	100	2.0
Case A3	200	200	1.0

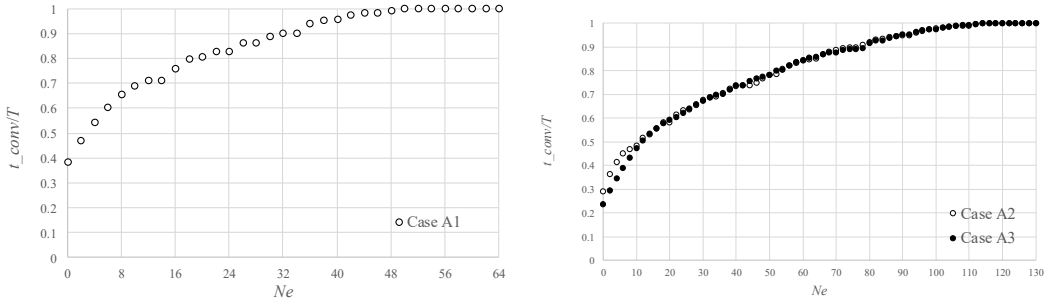

a) c=100 b) c=200

Fig. 7 Non-dimensional convergence time of ACFs with respect to N_e values

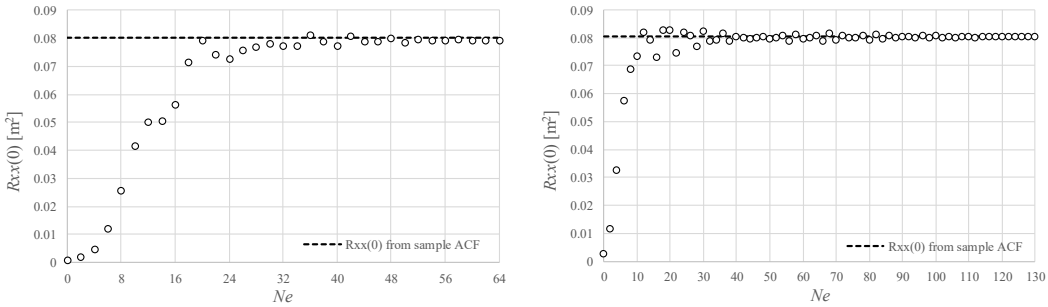

a) *Case A1* b) *Case A2*

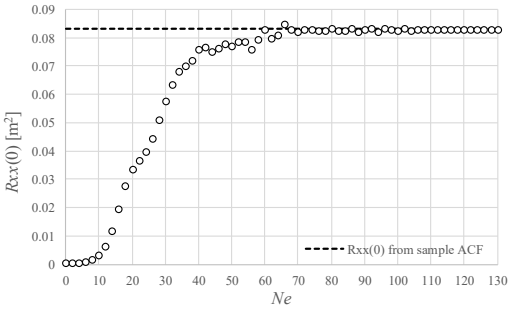

c) *Case A3*

Fig. 8 $R_{xx}(0)$ values by Method 2 with respect to N_e values

3.2.3 Method 2 vs. other methods

The ACF and/or PSD representation by Method 2 is compared with other PSD estimation methods, i.e. FFT and AR-based methods. In this paper, FFT is computed by using Matlab [30] without any smoothing of the PSD. The AR-based PSD estimation of which basic theories can be found from Akaike [31] and Neumaier and Schneider [32], for instance, is also adopted. The AR-based PSD estimation holds two advantages over FFT based one (cf. Penny [33]); 1) the power can be estimated over a continuous range of frequencies and 2) the power estimates have less variance. It is also well known that AR-based PSD gives

widely varying results depending on the method for deciding the AR model order. This study adopted a combination of Multiple Final Prediction Error (MFPE) and the Bayesian Information Criterion (BIC) criteria, which was used in Nielsen [34] for cross-spectrum estimates. The heave motion time series within $0 \le t \le t_0$ [s] where t_0=100, 200, or 500 [s] are used for a series of comparisons. To obtain ACF or PSD by Method 2, sample ACFs from $0 \le t \le t_0$ [s] measurements are calculated, and then PSWF-based smoothing is applied using the combination of c, T, and Ω as *Case A2* in Table 2. Moreover, N_e=50 is used in smoothing the ACFs. By applying N_e=50, it is expected that the ACFs are modified to be converged up to about t_conv/T=0.8, i.e. 80 [s], see Fig. 7 b). The ACFs from FFT and AR are calculated via the Wiener–Khinchin theorem by using the computed PSDs, see Eq. (11).

Fig. 9 shows a comparison of ACFs from Method 2, FFT and AR, respectively. The sample ACFs are shown with dotted lines in the figures. As found from the figures, the FFT-based ACFs show large amplitudes beyond the memory time of response, i.e. 80 [s]. To prevent this "failure of damping out" [13], smoothing process of PSD as demonstrated in Ref. [10] is necessary, but, as mentioned earlier, there is no consistent way to select the smoothing parameters. The AR based ACFs provide the decayed curve until certain time. However, a memory time indicated by the ACFs, i.e. time to converge to zero, is not consistently evaluated by the AR based ACFs. In other words, the expected memory time cannot be inferred by using AR-based methods.

Fig. 10 shows a comparison of PSDs from Method 2, FFT and AR, respectively. The Fourier transform from the sample ACFs (within $0 \le t \le 100$[s]) are also shown with dotted lines as a reference. It is evident that for the FFT-based PSDs from a short time window, e.g. t_0=100 [s], the frequency resolution is too low noting that the frequency resolution of FFT is based on the following relationship:

$$\Delta\omega = \frac{2\pi}{t_0} \tag{19}$$

Therefore, for t_0=100 [s], $\Delta\omega$ becomes 0.063 [rad/s] which covers only 16 discrete frequencies within $0 < \omega \le 1$ [rad/s] range, thus it is hard to capture the local spectrum peaks properly. On the other hand, the PSDs from Method 2 keep a high frequency resolution. This owes to a fact that the frequency resolution in Method 2 relies only on discretization of PSWF, equivalently dt/T in Eq. (14), which can be set arbitrarily in obtaining numerical values of PSWF. The AR-based PSDs keep a high frequency resolution with the smoothed PSD. But, the memory time of response is not observed clearly, as pointed above, and moreover, the estimated PSDs are single peaked, which may have been influenced by the selection method of the order of the AR model adopted in this study.

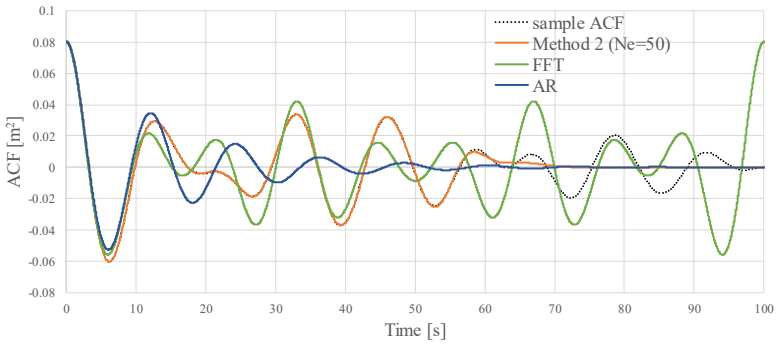

a) t_0=100 [s]

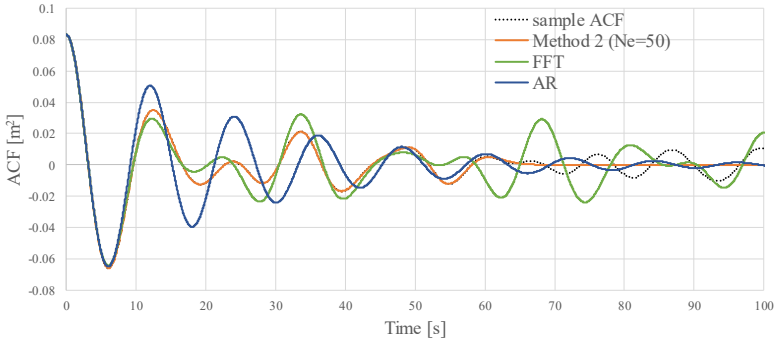

b) t_0=200 [s]

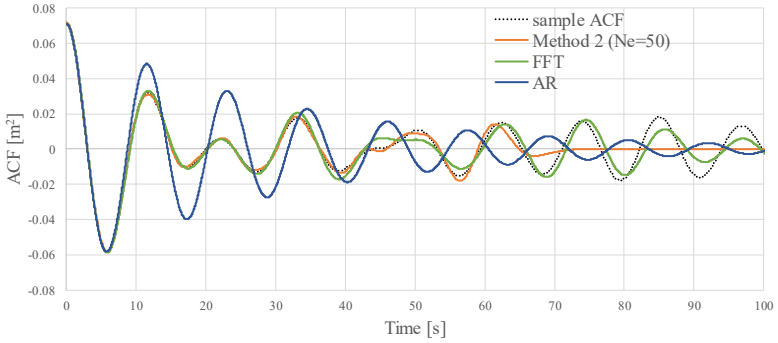

c) t_0=500 [s]

Fig. 9 Comparison of ACFs with Method 2, FFT and AR

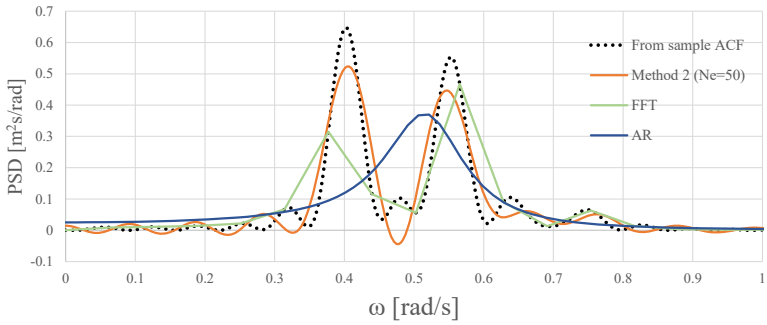

a) t_0=100 [s]

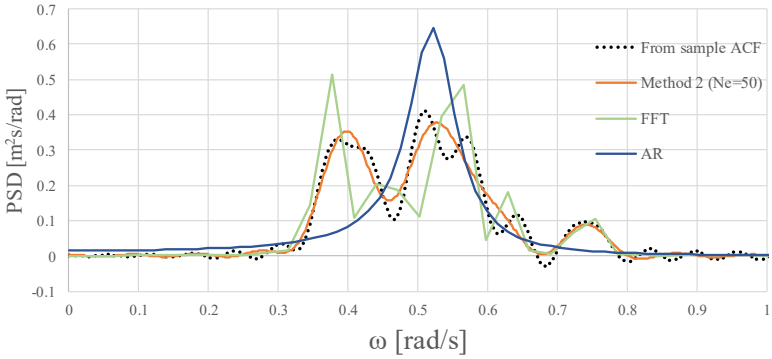

b) t_0=200 [s]

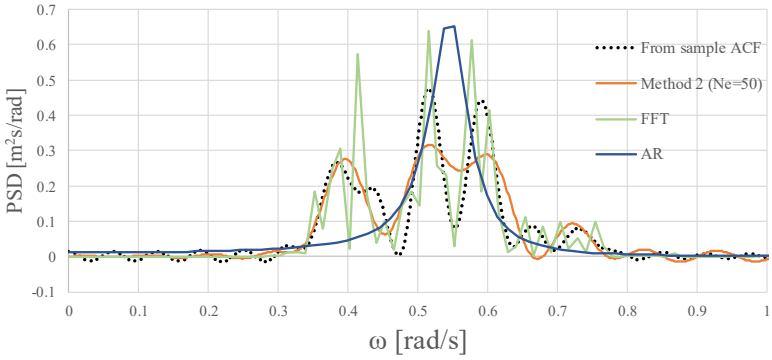

c) t_0=500 [s]

Fig. 10 Comparison of PSDs with Method 2, FFT and AR

3.3. ACF and PSD from Short Time Window

Next, Method 2 is applied to obtain the short-term variation of ACF and PSD within the whole time series in Fig. 4. The sample ACFs up to 100 seconds are calculated from time window length of 100, 200, 500, and 4000 [s] within whole time series of 4000 [s], then Method 2 using the combination of c, T, and Ω as in *Case A2* is applied to obtain the ACFs and PSDs. It should be noted that the short-term variability of the

time series may be included even in stationary time series, as presented in Hong et al. [12,35]. To investigate the short-term variability, the variance values from short time windows are first examined. Fig. 11 shows the variance values within different time windows, i.e. 100, 200, and 500 seconds, comparing with that from complete time sequence. It can be easily verified that the variance for short time windows, see 100 or 200 seconds, varies significantly. Obviously, this short-term variability leads to the large variation in the PSDs, as shown by Fig. A1 in Appendix B.

In light of the short-term variability of the time series, the ACFs and PSDs from short time windows are modified by accounting for the variance value σ^2, of the whole time span:

$$\bar{R}_{xx}(t) = \frac{\sigma^2}{R_{xx}(0)} R_{xx}(t)$$

$$\bar{S}_{xx}(\omega) = \frac{\sigma^2}{R_{xx}(0)} S_{xx}(\omega) \tag{20}$$

By applying Eq. (20), every single pair of ACF and corresponding PSD indicates the same variance value, i.e. σ^2.

Figs. 12-15 show the ACFs from 100, 200, 500, and 4000 [s] measurements, while Figs. 16-19 show the corresponding PSDs. The ACFs and /or PSDs by Method 2 are calculated like in subsection 3.2.3, i.e. using the combination of c, T, and Ω as *Case A2* with N_e=50. As a reference, sample ACFs themselves and PSDs from sample ACFs are shown in gray lines. The PSDs from the sample ACFs are calculated by using the sample ACFs within the period $0 \le t \le 100$[s]. In the plots, black thick lines indicate the input ACF and PSD of heave motion. When the time window size is long enough, say 4000 [s], the sample ACF becomes closer to the input ACF, and the resulting PSD is similar to the input PSD, see Fig. 12 a) and Fig. 16 a). However, relatively large fluctuations in the sample ACFs can be seen from short time windows, see Figs. 13-15 a). This (large) variation results in the large variation of PSDs, as can be observed from Figs. 17-19 a). On the other hand, PSWF-based smoothing results provide rather smoothed PSDs even for short time window cases, see Figs. 17-19 b). It is seen that the longer the time window length, the closer the evaluated PSD will be to the input PSD. This agreement is apparently owing to the smoothed ACFs.

It is envisioned that the present PSWF-based smoothing method, i.e. Method 2, enables a rapid updating of ACFs from short time measurements, without the need for long time sequences, along with a clear expression of the memory time of target response. In practice, the PSD of any response may be roughly approximated by using the transfer function and wave spectrum estimate, based on for example the wave-buoy analogy [36]. In this case, the memory time of the response may be roughly estimated from the inverse Fourier transform of the PSD. Subsequently, the present PSWF-based smoothing method can be applied so that the sample ACFs are modified to converge up to estimated memory time, as discussed in subsection 3.2.2.

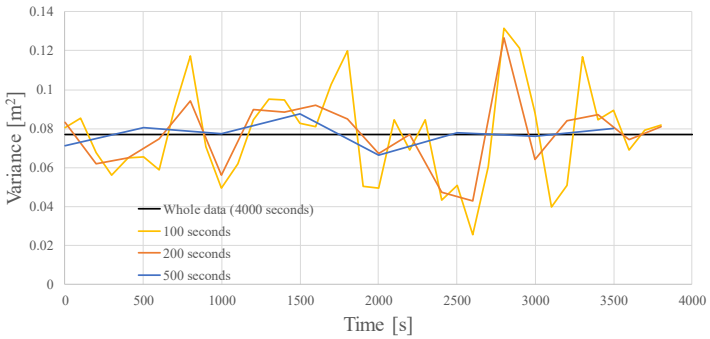

Fig. 11 Variance values for each time window

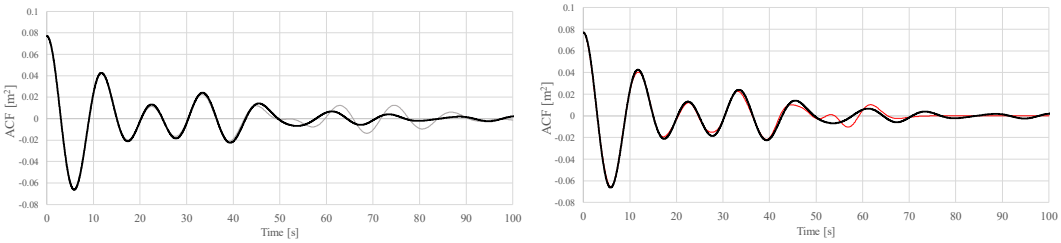

a) Sample ACF b) Method 2 (N_e=50)

Fig. 12 ACFs from time window length of 4000 seconds (whole data). Black thick line denotes the input ACF

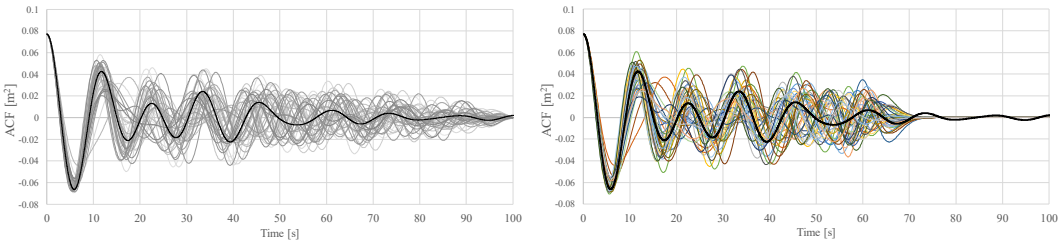

a) Sample ACF b) Method 2 (N_e=50)

Fig. 13 ACFs from time window length of 100 seconds. Black thick line denotes the input ACF

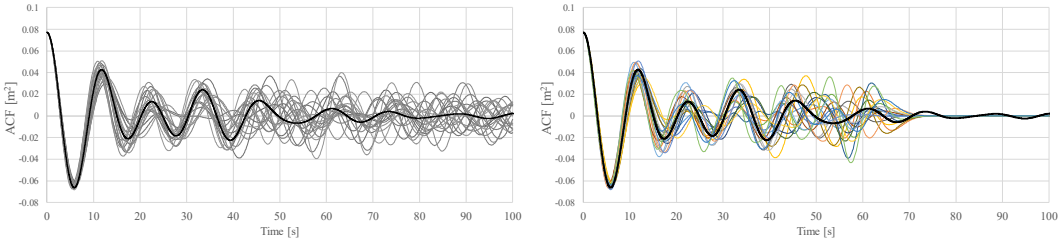

a) Sample ACF b) Method 2 (N_e=50)

Fig. 14 ACFs from time window length of 200 seconds. Black thick line denotes the input ACF

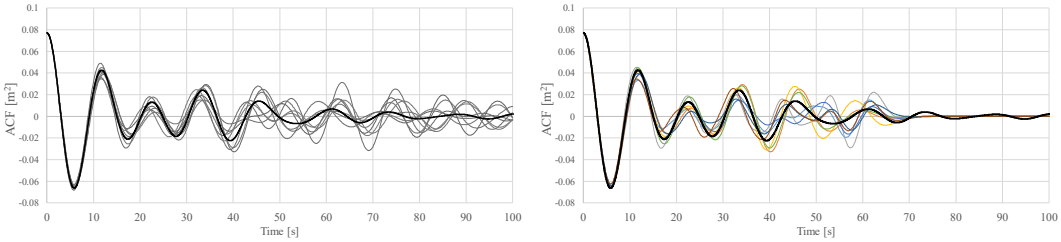

a) Sample ACF b) Method 2 (N_e=50)

Fig. 15 ACFs from time window length of 500 seconds. Black thick line denotes the input ACF

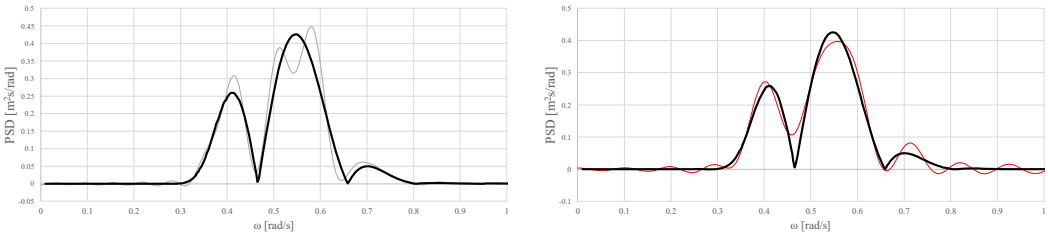

a) Fourier transform of sample ACF b) Method 2 (N_e=50)

Fig. 16 PSDs from time window length of 4000 seconds (whole data). Black thick line denotes the input PSD

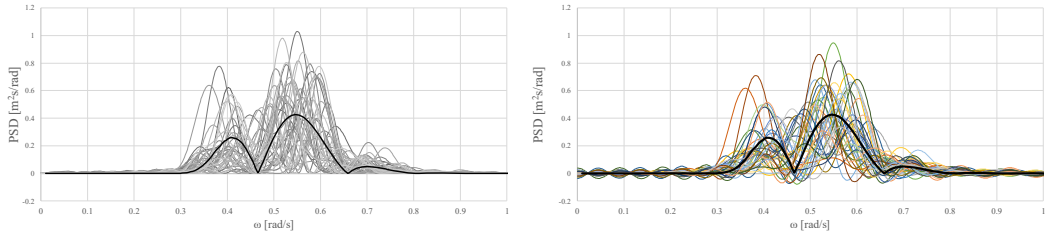

a) Fourier transform of sample ACF b) Method 2 (N_e=50)

Fig. 17 PSDs from time window length of 100 seconds. Black thick line denotes the input PSD

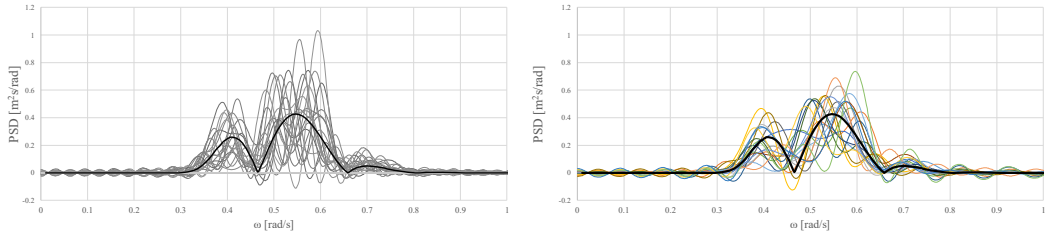

a) Fourier transform of sample ACF b) Method 2 (N_e=50)

Fig. 18 PSDs from time window length of 200 seconds. Black thick line denotes the input PSD

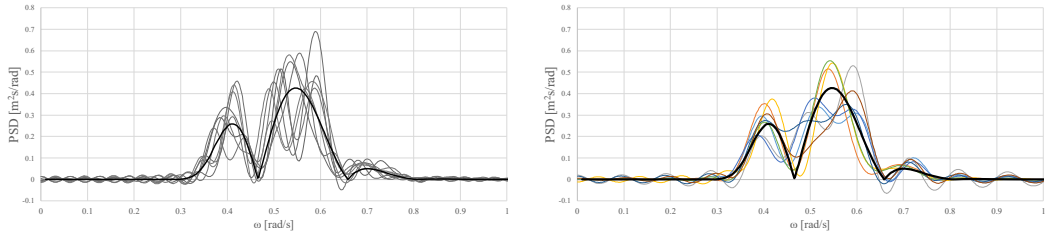

a) Fourier transform of sample ACF b) Method 2 (N_e=50)

Fig. 19 PSDs from time window length of 500 seconds. Black thick line denotes the input PSD

3.4. ACF-based Predictions Based on Method 2

In the last numerical demonstration, the effectiveness of the PSWF-based approach, using Method 2 to fit the ACF for response prediction [10,11] is investigated. The interested reader is referred to [10], but for completeness the following includes the basics of the prediction method. Thus, using the recent $n+1$ measurements, $x(t_0)$, $x(t_1)$,…, $x(t_n)$ where $t_0>t_1>\ldots>t_n$, the predictions at time t ahead of current time are given by:

$$\hat{x}(t) = \mathbf{r}^T(t)\mathbf{R}^{-1}\mathbf{x} \tag{21}$$

where $\mathbf{r}(t)$ denotes the autocorrelation vector, $\mathbf{R}$ the autocorrelation matrix, and $\mathbf{x}=[x(t_0), x(t_1),\ldots, x(t_n)]^T$ the measurement vector. In formulating the autocorrelation matrix, a noise term is normally included in order to reflect the inherent randomness in the measurements [37]. Herein, the noise terms are assumed to follow a normal distribution with mean 0 and variance σ_ε^2. Thereby, $\mathbf{r}(t)$ and $\mathbf{R}$ are given by the following form:

$$\mathbf{r}(t) = \left[r_{xx}(t-t_0) \quad r_{xx}(t-t_0+\Delta t) \quad \cdots \quad r_{xx}(t-t_0+n\Delta t) \right]^T$$

$$\mathbf{R} = \begin{bmatrix} 1+\dfrac{\sigma_\varepsilon^2}{R_{xx}(0)} & r_{xx}(\Delta t) & \cdots & r_{xx}(n\Delta t) \\ r_{xx}(\Delta t) & 1+\dfrac{\sigma_\varepsilon^2}{R_{xx}(0)} & \cdots & r_{xx}((n-1)\Delta t) \\ \vdots & \vdots & \ddots & \vdots \\ r_{xx}(n\Delta t) & \cdots & r_{xx}(\Delta t) & 1+\dfrac{\sigma_\varepsilon^2}{R_{xx}(0)} \end{bmatrix} \tag{22}$$

where

$$r_{xx}(t) = \frac{R_{xx}(t)}{R_{xx}(0)}$$

The time series data are down-sampled to 10Hz (Δt=0.1 [s]) in order to reduce the size of the autocorrelation matrix.

Using the smoothed ACFs by Method 2 with c, T, and Ω as set in *Case A2* (named 'PSWF-based ACF'), the ACF-based predictions starting from 2200 [s] are made. Predictions are made until 60 [s] ahead, i.e. up to 2260 [s], by using past 100 [s] measurements. The prediction results using the sample ACF (without noise) and PSWF-based ACF with N_e=50 derived from whole time measurements (from 0-4000 [s]) and recent 200 [s] measurements (from 2000-2200[s]) are first compared. Note that the sample ACF automatically includes unknown numerical noise for what reason the additional noise term, $\sigma_\varepsilon^2/R_{xx}(0)$ in Eq. (22), is not included in the sample ACF results. Fig. 20 shows the prediction results on the former case,

while Fig. 21 shows the latter case. From Fig. 20, one can find good predictions from PSWF-based ACFs and the sample ACFs when whole time measurements are used, especially within the first 20 [s]. The prediction accuracy using the sample ACF deteriorates when the recent 200 [s] measurements are used, as noted by the blue dotted line in Fig. 21.

Two metrics, the Pearson Correlation Coefficient ρ and the Determination Coefficient R^2 of the prediction results are calculated according to

$$\rho = \frac{\sum_{i=1}^{N_{pre}} (\hat{x}_i - \mu_{\hat{x}})(x_i - \mu_x)}{\sqrt{\sum_{i=1}^{N_{pre}} (\hat{x}_i - \mu_{\hat{x}})^2} \sqrt{\sum_{i=1}^{N_{pre}} (x_i - \mu_x)^2}} \tag{23}$$

$$R^2 = 1 - \frac{\sum_{i=1}^{N_{pre}} (\hat{x}_i - x_i)^2}{\sum_{i=1}^{N_{pre}} (x_i - \mu_x)^2} \tag{24}$$

where μ_x and $\mu_{\hat{x}}$ denote the mean values of measurements and predictions, respectively. N_{pre} is the number of predictions or measurements ahead, e.g. if ρ and R^2 are calculated until 60 [s] ahead, N_{pre}=600. ρ and R^2 corresponding to Figs. 20 and 21 are calculated and listed in Tables 3 and 4, respectively, where N_{pre} = 600 or 200. From Tables 3 and 4, the shorter prediction time, see N_{pre}=200 cases, offers better accuracy in both terms of ρ and R^2. It appears that the PSWF-based ACFs give better prediction results even if the recent 200 [s] measurements are used. This may be due to the fact that the sample ACF contains a large lag time error [13], whereas the PSWF can correct it. On the other hand, the prediction accuracy on the PSWF-based ACFs varies to a large degree depending on the variance of noise.

The prediction results at the other time window, starting from 970 [s], are shown in Fig. 22. Within the time window of 970-1030 [s], sudden increase of heave motion has been observed from measurements, see a black solid line in Fig. 22. When $\sigma_\varepsilon^2 / R_{xx}(0)$ of 0.1 or 0.01 are used for PSWF-based autocorrelation matrices, extremely large unrealistic oscillations appeared in the prediction results. In the present case, the determinant values of autocorrelation matrices **R** are extremely close to zero for every case, and such large oscillations appear in many noise level cases. $\sigma_\varepsilon^2 / R_{xx}(0)$ of 0.05 and 0.5 provide stable prediction time sequences. In Fig. 22, the recent 200 [s] measurements are used for obtaining ACFs, and the noise levels $\sigma_\varepsilon^2 / R_{xx}(0)$ of 0.05 and 0.5 are selected. Table 5 compares the two metrics in this case. It is again observed that the prediction accuracy by the PSWF-based ACF varies widely with the noise level, see Fig. 22 and Table 5. From Fig. 22, the sample ACF and PSWF-based ACF with $\sigma_\varepsilon^2 / R_{xx}(0)$= 0.05 can roughly capture the motion amplitude of the first wave, that is, up to about 17 [s] ahead, however, the accuracy is still low in terms of ρ and R^2 values, see Table 5.

It is inferred that the high variability in prediction accuracies by PSWF-based ACF results from the positive definiteness of the autocorrelation matrix **R** has not been secured in some cases. Although the inclusion of white noise is one of the ways to avoid non-positive definiteness of autocorrelation matrix [38],

further research effort should be paid to determine appropriate noise variance level or to modify the autocorrelation matrix **R**. The eigenvalue decomposition and selection of dominant eigenvalues in the autocorrelation matrix **R** would be one of the possible solutions [38]. Moreover, for practical reasons, a statistical evaluation of the prediction accuracy, e.g. evaluation of the peak value distribution or standard deviation, will be needed, and then the length of time for which the prediction accuracy is guaranteed should be clarified. Thus, it is early to draw definite conclusions on the accuracy of predictions by PSWF-based ACFs at this stage, necessitating future work. If an appropriate noise setting or autocorrelation matrix modification method can be established, since the present PSWF-based approach give reasonable ACFs for short time measurements, the method will be applicable to non-stationary time series, contrary to the conventional FFT based approach [10,11].

It would also be expected that the reference of confidence interval of sample ACF will be important for prediction accuracy, when the input PSD is unknown and only time series measurements are given under nonstationary operational conditions. The large-lag standard error [13] might be useful to determine a consistent lag time of sample ACF and may give an insight for determining PSWF settings. This point should also be investigated in the future.

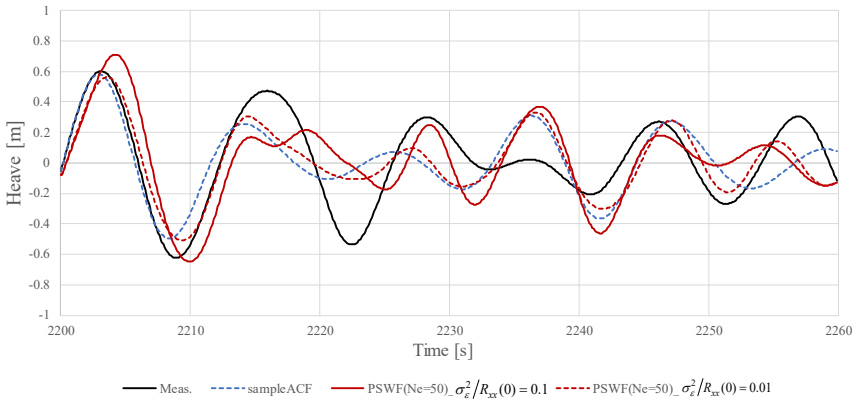

Fig. 20 Comparisons of ACF based prediction results starting from 2200 [s] between sample ACF and PSWF-based ACF with Gaussian noise. Sample ACF and PSWF-based ACF are calculated from whole time measurements (from 0-4000 [s])

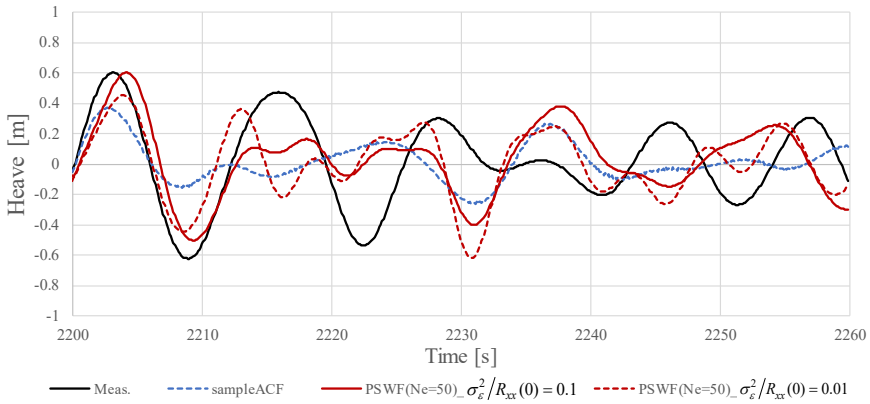

Fig. 21 Comparisons of ACF based prediction results starting from 2200 [s] between sample ACF and PSWF-based ACF with Gaussian noise. Sample ACF and PSWF-based ACF are calculated from recent 200 [s] measurements (from 2000-2200[s])

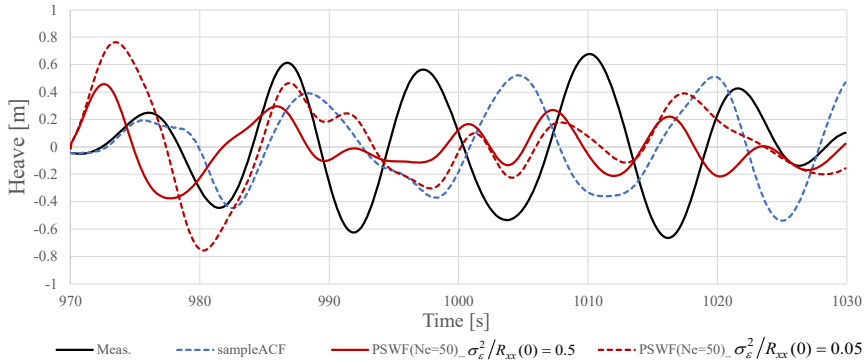

Fig. 22 Comparisons of ACF based prediction results starting from 970 [s] between sample ACF and PSWF-based ACF with Gaussian noise. Sample ACF and PSWF-based ACF are calculated from recent 200 [s] measurements (from 770-970[s])

Table 3 Comparison of the Pearson Correlation Coefficient ρ and the Determination Coefficient R^2 within 2200-2260 [s] when sample ACF and PSWF-based ACF are calculated from whole time measurements (from 0-4000 [s])

	Sample ACF	PSWF-based ACF ($\sigma_\varepsilon^2/R_{xx}(0)$=0.01)	PSWF-based ACF ($\sigma_\varepsilon^2/R_{xx}(0)$=0.1)
ρ (N_{pre}=600)	0.691	0.644	0.772
R^2 (N_{pre}=600)	0.472	0.329	0.595
ρ (N_{pre}=200)	0.915	0.828	0.954
R^2 (N_{pre}=200)	0.805	0.648	0.877

Table 4 Comparison of the Pearson Correlation Coefficient ρ and the Determination Coefficient R^2 within 2200-2260 [s] when sample ACF and PSWF-based ACF are calculated from recent 200 [s] measurements (from 2000-2200[s])

	Sample ACF	PSWF-based ACF ($\sigma_\varepsilon^2/R_{xx}(0)=0.01$)	PSWF-based ACF ($\sigma_\varepsilon^2/R_{xx}(0)=0.1$)
ρ (N_{pre}=600)	0.186	0.416	0.307
R^2 (N_{pre}=600)	-0.036	0.023	-0.142
ρ (N_{pre}=200)	0.630	0.860	0.682
R^2 (N_{pre}=200)	0.305	0.719	0.425

Table 5 Comparison of the Pearson Correlation Coefficient ρ and the Determination Coefficient R^2 within 970-1030 [s] when sample ACF and PSWF-based ACF are calculated from recent 200 [s] measurements (from 770-970[s])

	Sample ACF	PSWF-based ACF ($\sigma_\varepsilon^2/R_{xx}(0)=0.05$)	PSWF-based ACF ($\sigma_\varepsilon^2/R_{xx}(0)=0.5$)
ρ (N_{pre}=600)	-0.217	0.157	-0.059
R^2 (N_{pre}=600)	-0.973	-0.456	-0.298
ρ (N_{pre}=200)	0.705	0.696	0.229
R^2 (N_{pre}=200)	0.483	-0.354	-0.346

4. CONCLUSIONS AND FUTURE WORKS

This paper has presented a new approach for obtaining reliable autocorrelation functions (ACFs) and power spectrum densities (PSDs) from time series measurements. Specifically, Prolate Spheroidal Wave Functions (PSWF) were introduced to fit, respectively, a measured time series signal (Method 1) and the sample ACF (Method 2). A series of numerical demonstrations was made by using heave motion time series of a containership. The effectiveness of the present approach was discussed by comparing with other PSD estimation methods; herein Fast Fourier Transformation (FFT) and Auto-regressive (AR) based method, respectively. Finally, the present PSWF-based approach was applied to ACF-based deterministic time series prediction. The following conclusions can be drawn:

1. The sample ACF can be accurately reproduced by both Method 1 and Method 2, when a sufficient number of PSWF is considered. On the other hand, if the number is too low, the variance of the signal cannot be maintained by Method 1, and this leads to unreliable PSD estimation.
2. By applying Method2 with the appropriate number of PSWFs, the ACF converges up by a certain time, which is physically consistent with the response memory time. Meanwhile, a care should also be taken to choose large enough number of PSWFs to maintain the variance of the signal.

3. Method 2 enables provision of a high frequency resolution in the PSDs even if short time sequences of the measurements are used. Besides, the variability of PSD from short time sequences can be suppressed by converging the ACF to the memory time of response using Method 2.
4. By using the PSWF-based ACF by Method 2, it is expected that the PSWF-based ACF is capable of improving accuracy of deterministic motion prediction, since it makes it possible to correct the large-lag time error in the sample ACFs even if just the most recent short time sequences are used. However, it must be emphasized that further investigations will be needed to determine the appropriate noise variance level together with achieving positive definiteness of the autocorrelation matrix, which are highly associated with the large variation in results and prediction accuracy. Additional sensitivity studies and statistical evaluation of the prediction accuracy using Method 2, e.g. evaluation of standard deviation of predicted responses or peak value distributions, are therefore required in this line, and then it will be needed to clarify how long the predictions are practically accurate.

The potential for further applications of the proposed approach is suggested by the fact that, as the PSWF are adoptable for fitting band-limited signals, it may also be useful for *cross*-spectrum estimation, which is necessary for evaluating e.g. wave direction when ship motions are applied for sea state estimation using the wave buoy analogy [36,39]. This kind of application has particular interest, as it has been shown that short-term variations (“aleatory uncertainty”) in the seaway compromise results of the wave buoy analogy [35]. In this sense, it is expected that an improvement of the wave buoy analogy will be possible by introducing PSWF to estimate cross spectra during non-stationary sea states.

APPENDIX A: Derivation of PSWF

The numerical derivation of PSWF is made using the Legendre polynomials-based approach presented by Xiao et al. [20]. The Legendre polynomials P_n are defined by the three-term recursion,

$$P_{n+1}(u) = \frac{2n+1}{n+1} u P_n(u) - \frac{n}{n+1} P_{n-1}(u) \tag{A1}$$

with the initial conditions $P_0(u)=1$, $P_1(u)=u$. The numerical evaluation of PSWF can be made by:

$$\psi_j(u,c) = \sum_{k=0}^{\infty} \beta_k^j \overline{P}_k(u) \tag{A2}$$

where $\overline{P}_n$ is the normalized version of the Legendre polynomials, i.e.

$$\overline{P}_n(u) = P_n(u) \cdot \sqrt{n+0.5} \tag{A3}$$

For each j=0, 1, …, by denoting the coefficients β in Eq. (A2) as a column vector $\boldsymbol{\beta}^{\mathbf{j}}$,

$$\boldsymbol{\beta}^{\mathbf{j}} = (\beta_0^j, \beta_1^j, ...) \tag{A4}$$

The values in β^j are derived by solving the following algebraic eigenvalue problem.

$$(\mathbf{A} - \chi_j \cdot \mathbf{I})(\boldsymbol{\beta}^j) = 0 \tag{A5}$$

where χ_j denotes the eigenvalues corresponding to matrix **A**. The components in matrix **A** is given by

$$\begin{aligned} A_{k,k} &= k(k+1) + \frac{2k(k+1)-1}{(2k+3)(2k-1)} c^2 \\ A_{k,k+2} &= A_{k+2,k} = \frac{(k+1)(k+2)}{(2k+3)\sqrt{(2k+1)(2k+5)}} c^2 \\ otherwise, A &= 0 \end{aligned} \tag{A6}$$

To solve Eq. (A5) an eigenvalue solver based on the Jacobi's method can be applied. In practice, the number of k is limited to certain value, say, M. In this study, the cut-off number M is determined according to a suggestion given by Boyd [40],

$$M \geq 2N_e + 30 \tag{A7}$$

where N_e+1 denotes the number of PSWF to be evaluated. N_e is determined according to the value of Slepian frequency c so that the following condition is satisfied.

$$N_e + 1 \geq 2c/\pi \tag{A8}$$

After that, the scaled eigenvalues of each PSWF λ_j are calculated by using following relationships [22].

$$\begin{aligned} \lambda_{2k} &= (-1)^k \frac{\sqrt{2}\beta_0^{2k}}{\psi_{2k}(0,c)}, \quad k \geq 0 \\ \lambda_{2k+1} &= (-1)^k \sqrt{\frac{2}{3}} \frac{c\beta_1^{2k+1}}{\partial_u \psi_{2k+1}(0,c)}, \quad k \geq 0 \end{aligned} \tag{A9}$$

here ∂_u denotes the partial derivative in terms of u. Note that as the eigenvalues of PSWF μ_j should be less than 1, the absolute values of λ_j should be less than $\sqrt{2\pi/c}$.

APPENDIX B: PSD HISTORIES FROM DIFFERENT TIME WINDOWS

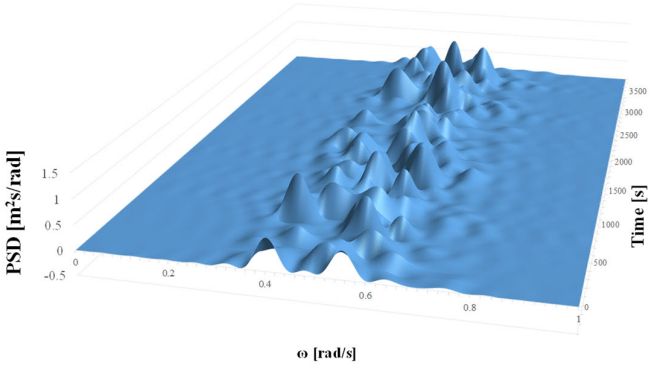

a) 100 seconds

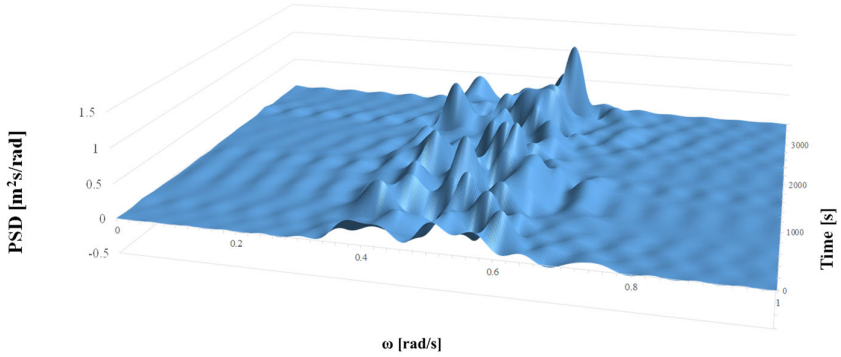

b) 200 seconds

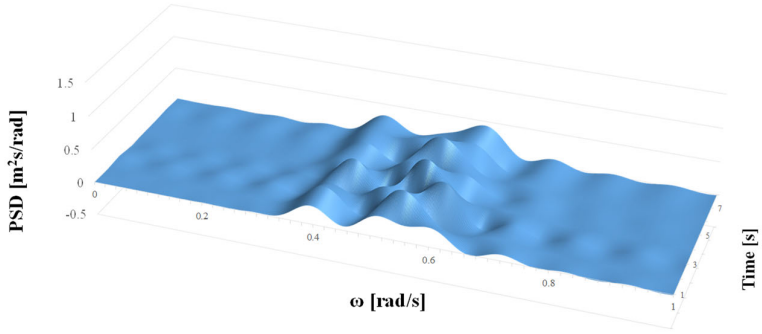

c) 500 seconds

Fig. A1 PSD histories of heave motion from different time window length

REFERENCES

[1] Chung JC, Bien Z, Kim YS. A Note on Ship-Motion Prediction Based on Wave-Excitation Input Estimation. IEEE J Ocean Eng 1990;15:244–50.

[2] Duan WY, Huang LM, Han Y, Wang R. IRF - AR model for short-term prediction of ship motion. Proc. Int. Offshore Polar Eng. Conf., 2015, p. 59–66.

[3] Huang L, Duan W, Han Y, Yu D, Elhandad A. Extending the Scope of AR Model in Forecasting Non-stationary Ship Motion by Using AR-EMD Technique. J Sh Mech 2015;19:1033–49.

[4] Duan W, Huang L, Han Y, Zhang Y, Huang S. A hybrid AR-EMD-SVR model for the short-term prediction of nonlinear and non-stationary ship motion. J Zhejiang Univ A 2015;16:562–76.

[5] Huang L, DUAN W, Han Y, Chen Y-S. A Review of Short-term Prediction Techniques for Ship Motions in Seaway. J Sh Mech 2014;18:1534–42.

[6] Sclavounos PD, Ma Y. Artificial intelligence machine learning in marine hydrodynamics. Proc. Int. Conf. Offshore Mech. Arct. Eng. - OMAE, vol. 9, 2018. doi:10.1115/OMAE2018-77599.

[7] Ma Y, Sclavounos PD, Cross-Whiter J, Arora D. Wave forecast and its application to the optimal control of offshore floating wind turbine for load mitigation. Renew Energy 2018;128:163–76.

[8] Duan S, Ma Q, Huang L, Ma X. A LSTM Deep Learning Model for Deterministic Ship Motions Estimation Using Wave-Excitation Inputs. Proc. Twenty-ninth Int. Ocean Polar Eng. Conf., 2019, p. 959–65.

[9] Andersen IMV, Jensen JJ, Nielsen UD. Evaluation of Response Prediction Procedures using Full Scale Measurements for a Container Ship. Proc. PRADS2013, 2013, p. 793–800.

[10] Nielsen UD, Brodtkorb AH, Jensen JJ. Response predictions using the observed autocorrelation function. Mar Struct 2018;58:31–52.

[11] Nielsen UD, Jensen JJ. Deterministic predictions of vessel responses based on past measurements. Proc. Int. Offshore Polar Eng. Conf., 2017, p. 513–9.

[12] Hong Y, Iseki T, Nielsen UD. Short-term Variability of Cross-Spectral Analysis for Ship Responses in Waves. Proc. Asia Navig. Conf. 2018, 2018, p. 1–6.

[13] Box GEP, Jenkins GM, Reinsel GC. Time Series Analysis: Forecasting and Control. 4th ed. Wiley; 2008.

[14] Slepian D, Pollak HO. Prolate spheroidal wave functions, fourier analysis and uncertainty - I. Bell Syst Tech J 1961;40:43–63.

[15] Lee G, Cho Y. Semi-analytical Karhunen–Loeve representation of irregular waves based on the prolate spheroidal wave functions. J Comput Phys 2018;352:172–89. doi:10.1016/j.jcp.2017.09.023.

[16] Sclavounos PD. Karhunen-Loeve representation of stochastic ocean waves. Proc R Soc A Math Phys Eng Sci 2012;468:2574–94. doi:10.1098/rspa.2012.0063.

[17] Khare K, George N. Sampling theory approach to prolate spheroidal wavefunctions. J Phys A Math Gen 2003;36:10011–21. doi:10.1088/0305-4470/36/39/303.

[18] Walter G, Soleski T. A new friendly method of computing prolate spheroidal wave functions and wavelets. Appl Comput Harmon Anal 2005;19:432–43. doi:10.1016/j.acha.2005.04.001.

[19] Cholewa M. Approximation of values of prolate spheroidal wave function. Theor Appl Informatics 2012;24:67–93. doi:10.2478/v10179-012-0004-5.

[20] Xiao H, Rokhlin V, Yarvin N. Prolate spheroidal wavefunctions, quadrature and interpolation. Inverse Probl 2001;17:805–38.

[21] Moore IC, Cada M. Prolate spheroidal wave functions, an introduction to the Slepian series and its properties. Appl Comput Harmon Anal 2004;16:208–30. doi:10.1016/j.acha.2004.03.004.

[22] Wang L-L. A Review of Prolate Spheroidal Wave Functions from the Perspective of Spectral Methods. J Math Study 2017;50:101–43.

[23] Boyd JP. Prolate spheroidal wavefunctions as an alternative to Chebyshev and Legendre polynomials for spectral element and pseudospectral algorithms. J Comput Phys 2004;199:688–

716.

[24] Jensen JJ, Mansour AE, Olsen AS. Estimation of shipmotions using closed-form expressions. Ocean Eng 2004;31:61–85.

[25] Mansour AE, Jensen JJ, Olsen AS. Fast Evaluation of the Reliability of Container Securing Arrangements. Proc. PRADS2004, 2004, p. 577–85.

[26] Van der Schaar M, Chou PA. Multimedia Over IP And Wireless Networks. 2007.

[27] Bendat JS, Piersol AG. Random Data : Analysis and Measurement Procedures. 4th ed. Wiley; 2010.

[28] Nielsen UD, Johannesen JR, Bingham HB, Blanke M, Joncquez S. Indirect Measurements of Added Wave Resistance on an In-service Container Ship. Proc. PRADS2019, 2019, p. T1-C–1.

[29] Kitagawa G. Introduction to Time Series Modeling. 1st ed. Chapman and Hall/CRC; 2010.

[30] Frigo M, Johnson SG. FFTW: an adaptive software architecture for the FFT. Proc. 1998 IEEE Int. Conf. Acoust. Speech Signal Process. ICASSP '98 (Cat. No.98CH36181), 1998.

[31] Akaike H. Autoregressive Model Fitting for Control. Ann Inst Stat Math 1971;23:163–80.

[32] Neumaier A. Estimation of Parameters and Eigenmodes of Multivariate Autoregressive Models. Acm Trans Math Softw 2001;27:27–57.

[33] Penny WD. Signal Processing Course. Lect. note, course Offer. Dep. Imaging Neurosci., 2000.

[34] Nielsen UD. Estimations of Directional Wave Spectra from Measured Ship Responses. Technical University of Denmark, 2005.

[35] Hong Y, Iseki T, Nielsen UD. The Effect of Short-term Variability of Cross-Spectral Analysis on Wave Buoy Analogy. Proc. Twenty-ninth Int. Ocean Polar Eng. Conf., 2019, p. 1311–8.

[36] Nielsen UD. A concise account of techniques available for shipboard sea state estimation. Ocean Eng 2017;129:352–62.

[37] Schulz E, Speekenbrink M, Krause A. A tutorial on Gaussian process regression: Modelling, exploring, and exploiting functions. J Math Psychol 2018;85:1–16.

[38] Mcmurry TL, Politis DN. High-dimensional autocovariance matrices and optimal linear prediction. Electron J Stat 2015;9:753–88.

[39] Nielsen UD, Dietz J. Ocean wave spectrum estimation using measured vessel motions from an in-service container ship. Mar Struct 2020;69:Article 102682.

[40] Boyd JP. Large mode number eigenvalues of the prolate spheroidal differential equation. Appl Math Comput 2003;145:881–6. doi:10.1016/S0096-3003(03)00280-7.